



HAL
open science

NuSTAR Observations of Candidate Subparsec Supermassive Black Holes

M. Lynne Saade, Murray Brightman, Daniel Stern, Thomas Connor, S.G Djorgovski, Daniel J d’Orazio, K.E.S Ford, Matthew J Graham, Zoltán Haiman, Hyunsung D Jun, et al.

► **To cite this version:**

M. Lynne Saade, Murray Brightman, Daniel Stern, Thomas Connor, S.G Djorgovski, et al.. NuSTAR Observations of Candidate Subparsec Supermassive Black Holes. *The Astrophysical Journal*, 2024, 966 (1), pp.104. 10.3847/1538-4357/ad372e . hal-04085031

HAL Id: hal-04085031

<https://hal.science/hal-04085031v1>

Submitted on 1 Dec 2024

HAL is a multi-disciplinary open access archive for the deposit and dissemination of scientific research documents, whether they are published or not. The documents may come from teaching and research institutions in France or abroad, or from public or private research centers.

L’archive ouverte pluridisciplinaire **HAL**, est destinée au dépôt et à la diffusion de documents scientifiques de niveau recherche, publiés ou non, émanant des établissements d’enseignement et de recherche français ou étrangers, des laboratoires publics ou privés.



Distributed under a Creative Commons Attribution 4.0 International License



NuSTAR Observations of Candidate Subparsec Binary Supermassive Black Holes

M. Lynne Saade^{1,2} , Murray Brightman³ , Daniel Stern⁴ , Thomas Connor⁵ , S. G. Djorgovski³ , Daniel J. D’Orazio⁶ , K. E. S. Ford^{7,8,9} , Matthew J. Graham³ , Zoltán Haiman¹⁰ , Hyunsung D. Jun¹¹ , Elias Kammoun^{12,13} , Ralph P. Kraft⁵ , Barry McKernan^{7,8,9} , Alexei Vikhlinin⁵ , and Dominic J. Walton^{14,15}

¹ Department of Physics and Astronomy, University of California, 475 Portola Plaza, Los Angeles, CA 90095, USA; mlysaade@usra.edu

² Science & Technology Institute, Universities Space Research Association, 320 Sparkman Drive, Huntsville, AL 35805, USA

³ Cahill Center for Astronomy and Astrophysics, California Institute of Technology, 1216 East California Boulevard, Pasadena, CA 91125, USA

⁴ Jet Propulsion Laboratory, California Institute of Technology, 4800 Oak Grove Drive, Pasadena, CA 91109, USA

⁵ Harvard-Smithsonian Center for Astrophysics, 60 Garden Street, Cambridge, MA 02138, USA

⁶ Niels Bohr International Academy, Niels Bohr Institute, Blegdamsvej 17, 2100 Copenhagen, Denmark

⁷ Department of Astrophysics, American Museum of Natural History, Central Park West at 79th Street, New York, NY 10024, USA

⁸ Department of Science, Borough of Manhattan Community College, City University of New York, New York, NY 10007, USA

⁹ Physics Program, The Graduate Center, City University of New York, New York, NY 10016, USA

¹⁰ Department of Astronomy, Columbia University, New York, NY 10027, USA

¹¹ SNU Astronomy Research Center, Astronomy Program, Department of Physics and Astronomy, Seoul National University, Seoul 08826, Republic of Korea

¹² IRAP, Université de Toulouse, CNRS, UPS, CNES 9, Avenue du Colonel Roche, BP 44346, F-31028, Toulouse Cedex 4, France

¹³ INAF–Osservatorio Astrofisico di Arcetri, Largo Enrico Fermi 5, I-50125 Firenze, Italy

¹⁴ Centre for Astrophysics Research, University of Hertfordshire, College Lane, Hatfield AL10 9AB, UK

¹⁵ Institute of Astronomy, University of Cambridge, Madingley Road, Cambridge CB3 0HA, UK

Received 2023 April 7; revised 2024 March 8; accepted 2024 March 22; published 2024 April 29

Abstract

We present an analysis of NuSTAR X-ray observations of three active galactic nuclei (AGN) that were identified as candidate subparsec binary supermassive black hole (SMBH) systems in the Catalina Real-Time Transient Survey based on apparent periodicity in their optical light curves. Simulations predict that close-separation accreting SMBH binaries will have different X-ray spectra than single accreting SMBHs. We previously observed these AGN with Chandra and found no differences between their low-energy X-ray properties and the larger AGN population. However, some models predict differences to be more prominent at energies higher than probed by Chandra. We find that even at the higher energies probed by NuSTAR, the spectra of these AGN are indistinguishable from the larger AGN population. This could rule out models predicting large differences in the X-ray spectra in the NuSTAR bands. Alternatively, it might mean that these three AGN are not binary SMBHs.

Unified Astronomy Thesaurus concepts: [Seyfert galaxies \(1447\)](#); [X-ray active galactic nuclei \(2035\)](#); [Quasars \(1319\)](#); [Supermassive black holes \(1663\)](#)

1. Introduction

Binary supermassive black holes (SMBHs) are expected to be a ubiquitous consequence of galaxy mergers. When two galaxies merge, their corresponding SMBHs will pair up into binaries. The binary separation will shrink due to gravitational interactions with stars (Berczik et al. 2006; Gualandris et al. 2017) and gas (Mayer et al. 2007) in the merged galaxy. When the binary reaches subparsec separation, gravitational waves become the dominant mode by which the binary shrinks, allowing the two black holes to spiral together and merge (Begelman et al. 1980). In the process, they will release gravitational waves that could be detected by future observatories such as the Laser Interferometric Space Antenna (Amaro-Seoane et al. 2017, 2023), as well as pulsar timing arrays (Xin et al. 2021).

Candidate binary SMBHs have been identified in active galactic nuclei (AGN) through a variety of methods, including unusual jet morphologies (e.g., Lobanov & Roland 2005; Caproni et al. 2013; Tsai et al. 2013; Kun et al. 2014; Krause et al. 2019), emission line profiles (e.g., Eracleous et al. 2012; Ju et al. 2013; Shen et al. 2013; Liu et al. 2014; Li et al. 2016;

Guo et al. 2019), candidate periodic features in AGN light curves (e.g., Lehto & Valtonen 1996; Graham et al. 2015a, 2015b; Charisi et al. 2016; Liu et al. 2019; Chen et al. 2020, 2024; Liao et al. 2021; O’Neill et al. 2022), and X-ray variability (e.g., Liu et al. 2020; Serafinelli et al. 2020). For a recent review of this field, see Bogdanović et al. (2022). Of the candidates identified, the current strongest candidate is OJ 287, which displays periodic flares that are well explained by a model in which a secondary black hole passes through a primary black hole’s accretion disk once per decade (Lehto & Valtonen 1996). This model has been used to predict a flare in OJ 287 down to the precision of a day (Valtonen et al. 2008). A flare was observed in 2020 that is consistent with the binary model (Komossa et al. 2020). However, a predicted flare in 2022 was not seen, and the disk luminosity was found to be a factor of 10–100 times lower, indicating that some aspects of the original model need modification, such as including precession and/or considering a lower mass for the primary SMBH (Komossa et al. 2023).

The second strongest candidate is PG 1302–102, which shows some evidence for consistent periodicity in its optical (Graham et al. 2015a), ultraviolet (D’Orazio et al. 2015; Xin et al. 2020), and mid-infrared light curves (Jun et al. 2015), as well as in the precession of its radio jet (Qian et al. 2018). In particular, the ratio of the amplitudes in the UV and optical matches expectations under the assumption that the sinusoidal



Original content from this work may be used under the terms of the [Creative Commons Attribution 4.0 licence](#). Any further distribution of this work must maintain attribution to the author(s) and the title of the work, journal citation and DOI.

Table 1
Target Sample and Observation Details

Target	Observatory	ObsID	Date	Net Exposure Time (ks)	Net Count Rate (counts ks ⁻¹)
2MASXi J0729087+400836	Chandra	19528	2017-04-28	7.6	267.5
	NuSTAR	60601029002	2021-05-16	21.5/21.3	44.2/40.0
PG 1302–102	Swift	00089146001	2021-06-08	1.7	144.7
	NuSTAR	60601030002	2021-06-08	36.5/36.3	68.1/65.7
FBQS J163302.6+234928	XMM-Newton	0870910101	2020-08-08	57.6/5.8/3.6	537.7/118.5/146
		0870910301	2021-01-31	73.49/199.4/103.8	748.4/199.9/195.6
	NuSTAR	60601012002	2020-08-09	102.2/101.2	21.2/19.5
		60601012004	2021-01-31	101.1/100.0	22.9/20.8

Note. NuSTAR net exposure times and net count rates are written as FPMA/FPMB. XMM-Newton net exposure times and net count rates are written as pn/MOS1/MOS2.

variation is due to relativistic Doppler modulation from binary orbital motion given the UV and optical spectral slopes (D’Orazio et al. 2015; Xin et al. 2020).

Another potential way to detect binary SMBHs is through X-ray emissions. Since X-rays probe the portion of an AGN closest to the central black hole(s), the presence of a subparsec SMBH binary could potentially have a large imprint on the high-energy emission. Several models have predicted the X-ray emissions of binary SMBH AGN, though they differ in their predictions in part because current simulations are unable to simulate thin disks and thus make ad hoc approximations about the thermodynamics. Some analyses predict a notch in the X-ray spectrum (e.g., Tang et al. 2018) and/or for the spectral shape of the high-energy continuum to be harder (e.g., Roedig et al. 2014; Ryan & MacFadyen 2017; Tang et al. 2018; Krolik et al. 2019), while others predict more modest differences, if any (e.g., d’Ascoli et al. 2018; Gutiérrez et al. 2022). Many models predict increased X-ray luminosity as well (e.g., 10x higher in the 10–100 keV band; Farris et al. 2015).

In our previous paper, Saade et al. (2020, hereafter SA20), we observed seven AGN identified as potentially periodic by Graham et al. (2015b) from the Catalina Real-Time Transient Survey (Drake et al. 2009). We used Chandra observations to test theoretical models of accreting binary SMBHs and potentially determine whether the AGN were binary SMBHs. We did not find any significant differences between the spectra of these AGN and the spectra of single SMBH AGN. While there are many possible reasons for this result (discussed at length in SA20), one potential reason is that the differences in X-rays could be modest in the soft X-rays but more dramatic in the harder X-rays, as predicted by some calculations (e.g., Roedig et al. 2014).

Three of the AGN in SA20 have NuSTAR (Harrison et al. 2013) observations through a combination of our own proposal and archival data. In this work, we analyze these NuSTAR spectra to see if there is any evidence that the predicted differences between binary SMBH AGN and single SMBH AGN show up in the hard X-rays. The structure of our paper is as follows. In Section 2, we describe the X-ray data and reduction thereof. In Section 3, we discuss the X-ray properties of our sample and compare it to other samples in the literature. In Section 4, we discuss the implications of our results in the context of both theory and observations. For calculating the luminosities, we use the cosmology used in NASA’s Extragalactic Database (NED), namely, $\Omega_M = 0.308$, $\Omega_\Lambda = 0.692$, and $H_0 = 67.8 \text{ km s}^{-1} \text{ Mpc}^{-1}$.

2. Observations and Data Analysis

The X-ray observations used in this paper are listed in Table 1. We use all available NuSTAR data for the objects in the SA20 sample. This amounted to three objects: 2MASXi J0729087+400836, PG 1302–102, and FBQS J163302.6+234928. 2MASXi J0729087+400836 and PG 1302–102 have NuSTAR data from our Cycle 6 proposal (PI: M. Saade). The FBQS J163302.6+234928 NuSTAR observations were obtained from the archive (PI: E. Kammoun).

For soft X-ray data, we preferentially used data taken simultaneously with NuSTAR. For PG 1302–102, this was Swift (Gehrels et al. 2004) data; for FBQS J163302.6+234928, this was XMM-Newton (Jansen et al. 2001) data. 2MASXi J0729087+400836 did not have any simultaneous observations, so we reuse the Chandra (Weisskopf et al. 2002) observation reported in SA20. All the high-energy observations were background-subtracted and fit in XSPEC (Arnaud 1996, version 12.12.1). The spectra were grouped by a minimum of 1 count bin⁻¹. In this situation, XSPEC uses a modified version of the C-statistic known as the W-statistic. Below, we describe the specific details of each observatory’s data analysis.

2.1. NuSTAR

We reduced and extracted the NuSTAR data with HEASOFT (version 6.30.1), NuSTARDAS (version 2.1.2), and NuSTAR CALDB (version 20220525). We used 40'' radius circular regions centered on each source for the extraction and 100'' radius background regions. In fitting the spectra of 2MASXi J0729087+400836 and PG 1302–102, we fixed the cross-normalization constant of FPMA to 1.0 and that of FPMB to 1.04, where the latter is based on calibration observations of the bright source 3C 273 reported in Madsen et al. (2015). We also did this for the first NuSTAR observation of FBQS J163302.6+234928. For the second observation of FBQS J163302.6+234928, we let the FPMA constant freely vary and fixed the FPMB constant to be 1.04× the FPMA constant. The NuSTAR background dominates the source above 30 keV, so we used the 3–30 keV range for the spectral fitting.

2.2. Swift

The HEASARC archive includes a Swift observation contemporaneous with the NuSTAR observation of PG 1302–102. We reduced and extracted the X-Ray Telescope (XRT) data with HEASOFT (version 6.30.1), the Swift XRT

CALDB (version 20210915), and the Swift XRT Data Analysis Software (version 3.7.0). We used a circular source region of $25''$ radius and a circular background region of $50''$ radius. We used the 0.3–10 keV range for the spectral fitting.

2.3. XMM-Newton

FBQS J163302.6+234928 has a simultaneous XMM-Newton observation for both NuSTAR observations. We extracted the data using the XMM-Newton Scientific Analysis Software (version 20.0.0). For all XMM-Newton cameras, we used circular source regions $20''$ in radius. We used a circular background region $80''$ in radius for the MOS cameras and $60''$ in radius for the pn camera. The latter was smaller in order to avoid chip edges and extra sources.

For all XMM-Newton observations, we filtered out times with high background, defined as when the count rate in the 10–12 keV range was >0.4 counts s^{-1} for the pn and >0.35 counts s^{-1} for the MOS cameras. The first observation suffered from a large background flare, with count rates of up to 18 counts s^{-1} in the pn camera and 7–8 counts s^{-1} in the MOS cameras. The flare continued for longer in the MOS cameras, such that while only 45% of the pn exposure time was lost due to background flaring, 78% of the MOS1 exposure time and 85% of the MOS2 exposure time was lost to background flaring. In addition to background flaring, a known flare star (2MASS J16330429+2349464) was present $30''$ away from the quasar in the pn image. To avoid the star, we extracted the pn, MOS1, and MOS2 spectra using $20''$ radius source regions that did not include the star.

The second observation had discrete background flares instead of the overall high levels of the first observation, resulting in less time lost to background flares. Specifically, 30% of the pn exposure time, 2% of the MOS1 exposure time, and 3% of the MOS2 exposure time were lost to background flaring. The flare star appeared in all three cameras even after background flare filtering. To avoid activity from the flare star, we also extracted the pn, MOS1, and MOS2 spectra of the second XMM-Newton observation using $20''$ radius source regions.

2.4. Chandra

For 2MASXi J0729087+400836, there were no soft X-ray observations contemporaneous with the NuSTAR observation, so we used the earlier Chandra data reported in SA20 (ObsID: 10.25574/19528). We used the spectra from that paper, grouped to have a minimum of 1 count bin^{-1} . This was done using CIAO version 4.10 with CALDB version 4.8.0. The spectrum was extracted with a circular source region $2''$ in radius, with an annular background region centered on the source of inner radius $10''$ and outer radius $20''$. We used energies of 0.5–8.0 keV for the spectral fitting.

3. X-Ray Properties

3.1. Average Spectra

The unfolded spectra of the AGN are shown as the error bars in Figures 1, 2, and 3. We first considered average spectra. We fit all three average spectra with a CONSTANT*TBABS*ZPHABS*CUTOFFPL model, with the CONSTANT term representing the cross-normalization constant between multiple observations, TBABS representing photoelectric absorption

within our Galaxy, ZPHABS representing photoelectric absorption in the host galaxy, and the CUTOFFPL model representing the intrinsic spectrum of the black hole corona, which radiates approximately as a power-law spectrum with an exponential cutoff. To take into account reflection components, we also tried a CONSTANT*TBABS*ZPHABS*(CUTOFFPL+PEXRAV) model, where the PEXRAV (Magdziarz & Zdziarski 1995) parameter R was set to be less than 0 to ensure it represented the reflection component only. We fixed the inclination to be 30° , the CUTOFFPL norm to be equal to the PEXRAV norm, and the CUTOFFPL gamma to be the PEXRAV gamma. This left R as the only free parameter in the fit. FBQS J163302.6+234928 in particular appears to have a strong reflection component, and its fit substantially benefits from the addition of a PEXRAV component. In contrast, 2MASXi J0729087+400836 and PG 1302–102 did not show much improvement in C-stat/dof with the addition of a PEXRAV component. For this reason, we use the CONSTANT*TBABS*ZPHABS*CUTOFFPL fits as the best fits for these two sources, while we use the fit with PEXRAV for FBQS J163302.6+234928. The best fits to the average spectra, along with their C-stat/dof and the observed NuSTAR FPMA fluxes, are presented in Table 2. The average spectra are well fit by the best-fit models, with C-stat/dof values of ≈ 1 , though 2MASXi J0729087+400836 shows some soft excess above the power-law component, a feature found in most AGN spectra below about 2 keV (Ballantyne & Xiang 2020). The physical origin of this soft excess is not clear but has been proposed to be smeared reflected emission lines (Crummy et al. 2006; Walton et al. 2013) or a warm (~ 0.1 keV) component of the corona (Mehdipour et al. 2011; Done et al. 2012). 2MASXi J0729087+400836 shows $\sim 40\%$ variability between its Chandra and NuSTAR observations. FBQS J163302.6+234928 shows $\sim 50\%$ variability between its two XMM-Newton observations and 7% variability between its two NuSTAR observations.

From the best-fit XSPEC models, we measure the average spectral index, Γ , for the three AGN. Taking into account the NuSTAR data, the values are softer than measured in the Chandra data alone in SA20. This is particularly true for FBQS J163302.6+234928, likely because of the addition of the reflection component compared to the fit from SA20. There is overlap between the 90% confidence intervals for Γ from SA20 and this paper for 2MASXi J0729087+400836 and PG 1302–102, meaning these measurements are consistent with each other. The same is not true for FBQS J163302.6+234928's value of Γ , which does not overlap with its 90% confidence interval from SA20. PG 1302–102's Γ is within the 1.5–2.0 range typical for AGN (Nandra & Pounds 1994; Shemmer et al. 2008; Brightman et al. 2013). However, 2MASXi J0729087+400836 has slightly harder values of Γ than the typical range, while FBQS J163302.6+234928 has a slightly softer value of Γ than typical. The value of the PEXRAV R for FBQS J163302.6+234928 is extremely high ($7.67_{-1.30}^{+1.38}$), much larger than the typical 1–2 range for AGN, implying a very hard spectrum. Similarly high values, however, were found for a few sources in Ricci et al. (2017); e.g., Mrk 1310 is best fit with $R=6.7$, and ESO 438-9 is best fit with $R=7.8$. We attempted to set an upper limit of 2 on R and refit to see if the value of Γ would also become hard. However, the value of Γ only went down to $2.12_{-0.01}^{+0.02}$, which is still soft. We also tried ignoring the energies below 2 keV to avoid the

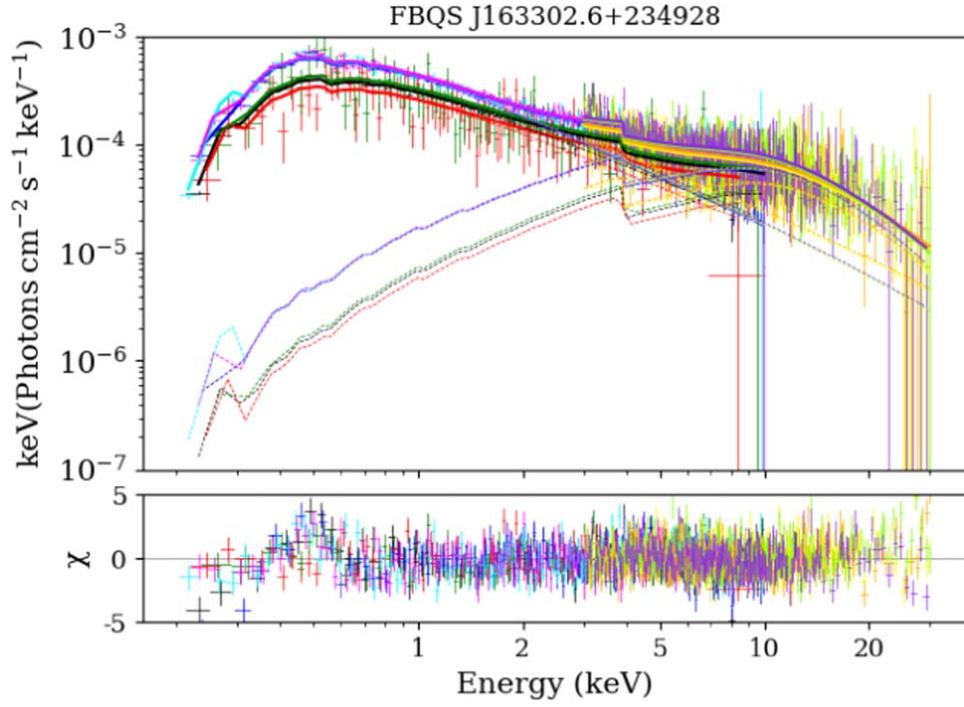


Figure 1. Unfolded spectrum and best-fit TBABS*ZPHABS*(CUTOFFPL+PEXRAV) model for FBQS J163302.6+234928. Black, red, and green correspond to pn, MOS1, and MOS2 data from XMM-Newton observation 0870910101. Blue, cyan, and magenta correspond to pn, MOS1, and MOS2 data from XMM-Newton observation 0870910301. Yellow and orange correspond to FPMA and FPMB data from NuSTAR observation 60601012002. Chartreuse and purple correspond to FPMA and FPMB data from NuSTAR observation 60601012004. The model plotted is the fit reported in Table 3.

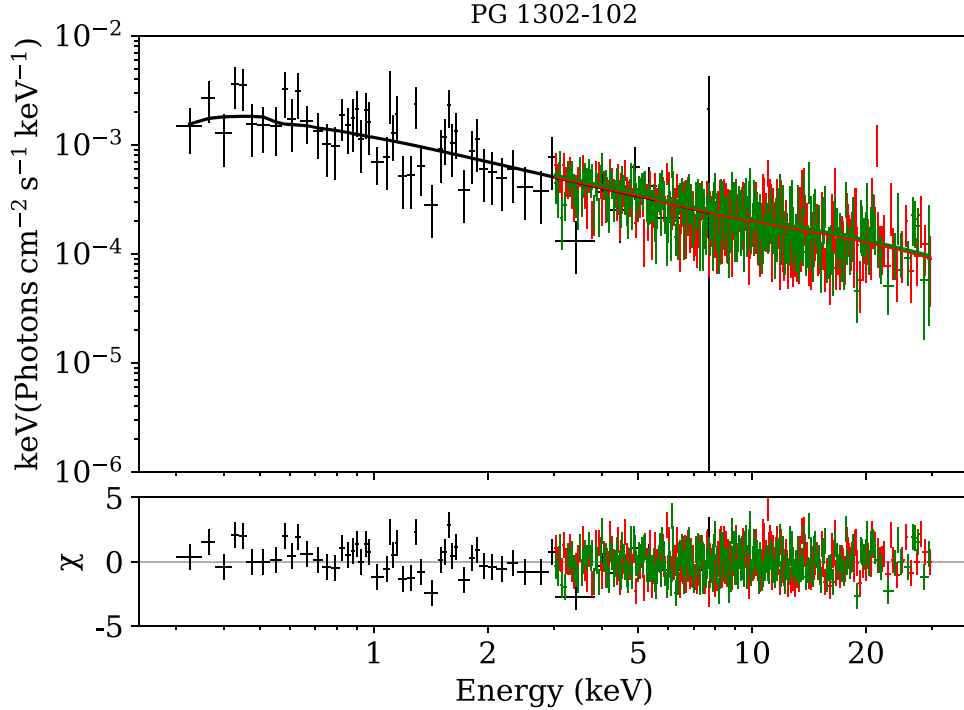


Figure 2. Unfolded spectrum and best-fit TBABS*ZPHABS*CUTOFFPL model for PG 1302-102. Black corresponds to Swift XRT data; red and green correspond to NuSTAR FPMA and FPMB data. The model plotted is the fit reported in Table 2.

possibility of any soft excess biasing the value of Γ . In this case, Γ went down only to 2.02 ± 0.10 , which is still soft.

We compare the spectral indices of our sample from the average spectral fits to the spectral indices of the BAT AGN Spectroscopic Survey (BASS) sample (Ricci et al. 2017). This sample includes 838 AGN. We exclude the blazars from the

sample, as they have different X-ray spectra than nonblazar AGN. Excising the blazars, the sample contains 703 AGN at redshift $0.001 \leq z \leq 0.65$, with bolometric luminosities $39.54 \leq \log(L_{\text{bol}}/\text{erg s}^{-1}) \leq 47.75$. The BASS sample properties envelope the three targets discussed here. The Γ values for our sample measured using the TBABS*ZPHABS*(CUTOFFPL

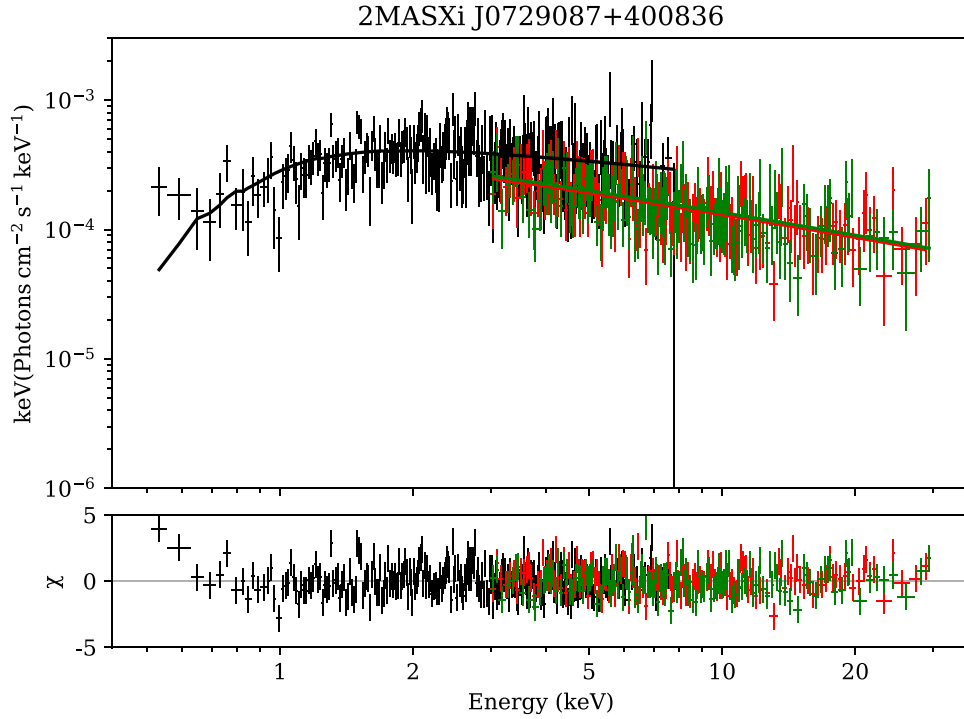


Figure 3. Unfolded spectrum and best-fit TBABS*ZPHABS*CUTOFFPL model for 2MASXi J0729087+400836. Black corresponds to Chandra data; red and green correspond to NuSTAR FPMA and FPMB data. The model plotted is the fit reported in Table 4.

Table 2
Parameters for Best-fit Average Models

Target	ZPHABS	CUTOFFPL			PEXRAV	C-stat/dof	Observed Flux (10^{-13} erg cm^{-2} s^{-1})
	N_{H} (10^{22} cm^{-2})	Γ	E_{cut} (keV)	Norm (10^{-4} counts s^{-1} keV^{-1})	R		
2MASXi J0729087+400836	$0.24^{+0.10}_{-0.09}$	$1.40^{+0.13}_{-0.16}$	>30.05	$3.85^{+0.84}_{-0.69}$	N/A	1036.67/1143	21.9 ± 1.0
PG 1302-102	<0.01	1.72 ± 0.05	>186.62	$10.98^{+1.01}_{-1.01}$	N/A	1103.37/1121	$39.8^{+1.9}_{-1.8}$
FBQS J163302.6+234928	0.14 ± 0.01	2.36 ± 0.05	$66.73^{+15.73}_{-10.94}$	$4.64^{+0.17}_{-0.16}$	$7.67^{+1.38}_{-1.30}$	3114.70/2914	$8.51^{+0.20}_{-0.19}$, $9.36^{+0.57}_{-0.55}$

Note. Error bars represent 90% confidence intervals. For 2MASXi J0729087+400836 and PG 1302-102, a TBABS*ZPHABS*CUTOFFPL model provided a satisfactory fit; for FBQS, a TBABS*ZPHABS*(CUTOFFPL+PEXRAV) fit was necessary. In fits with PEXRAV components, abundances were set to solar, the PEXRAV cutoff energy was set equal to the CUTOFFPL cutoff energy, and the PEXRAV norm was set equal to the CUTOFFPL norm, leaving R as the only free PEXRAV parameter. For observed fluxes, the NuSTAR FPMA flux of the best average fit was used. The Chandra normalization constant value for 2MASXi J0729087+400836 was $1.71^{+0.16}_{-0.15}$ (ObsID: 19528). The Swift XRT normalization constant for PG 1302-102 was $1.08^{+0.15}_{-0.14}$ (ObsID: 00089146001). The XMM-Newton normalization constants for the first observation of FBQS J163302.6+234928 (ObsID: 0870910101) were 0.77 ± 0.03 for pn, 0.67 ± 0.05 for MOS1, and $0.83^{+0.07}_{-0.06}$ for MOS2. The XMM-Newton normalization constants for the second observation of FBQS J163302.6+234928 (ObsID: 0870910301) were 1.11 ± 0.04 for pn, 1.12 ± 0.04 for MOS1, and 1.13 ± 0.04 for MOS2. The NuSTAR FPMA constant for the second observation of FBQS J163302.6+234928 (ObsID: 60601012004) was 1.14 ± 0.04 .

+PEXRAV) average spectral fits are compared to the BASS Γ values in their Table 5. The BASS values of Γ were measured using a PEXRAV component with a CUTOFFPL input freely fit; therefore, they take into account both an intrinsic continuum and a reflection component. We use the PEXRAV-containing fits of our three AGN for comparison even though they are not required for 2MASXi J0729087+400836 and PG 1302-102. This is in order to be consistent with the BASS spectral model and to use our full sample in the comparison. We performed a Kolmogorov-Smirnov (KS) test comparing the three candidate binary SMBH sources grouped together as a distribution against the BASS sample, making a cut to the BASS sample based on Eddington ratio. For the BASS sample, we use the Eddington ratios from Koss et al. (2017), preferentially using values calculated based on Swift 14-195 keV luminosity, when available. In cases where this was not available, we used the Eddington ratios calculated from the

5100 Å luminosity. A total of 319 AGN in the BASS sample have Eddington ratios measured in these two ways. We restricted the Eddington ratio to be $-1.08 \leq \log(L/L_{\text{Edd}}) \leq -0.12$, leaving a sample of 170 AGN to compare to our three AGN with a KS test. The resulting p -value of 0.867 is too high to reject the null hypothesis that our three candidate binary SMBH AGN are drawn from the same distribution as the BASS sample. This is the same conclusion we came to in SA20 for a larger sample with only soft X-ray data.

We then investigated how the sample compares to the general AGN population when including NuSTAR data above 10 keV. For this comparison, we compared the average spectral indices of our sample against the sample of 195 unobscured AGN in Kamraj et al. (2022). These AGN are a subset of the BASS sample and have NuSTAR observations in addition to Swift XRT and XMM-Newton observations. We cross-

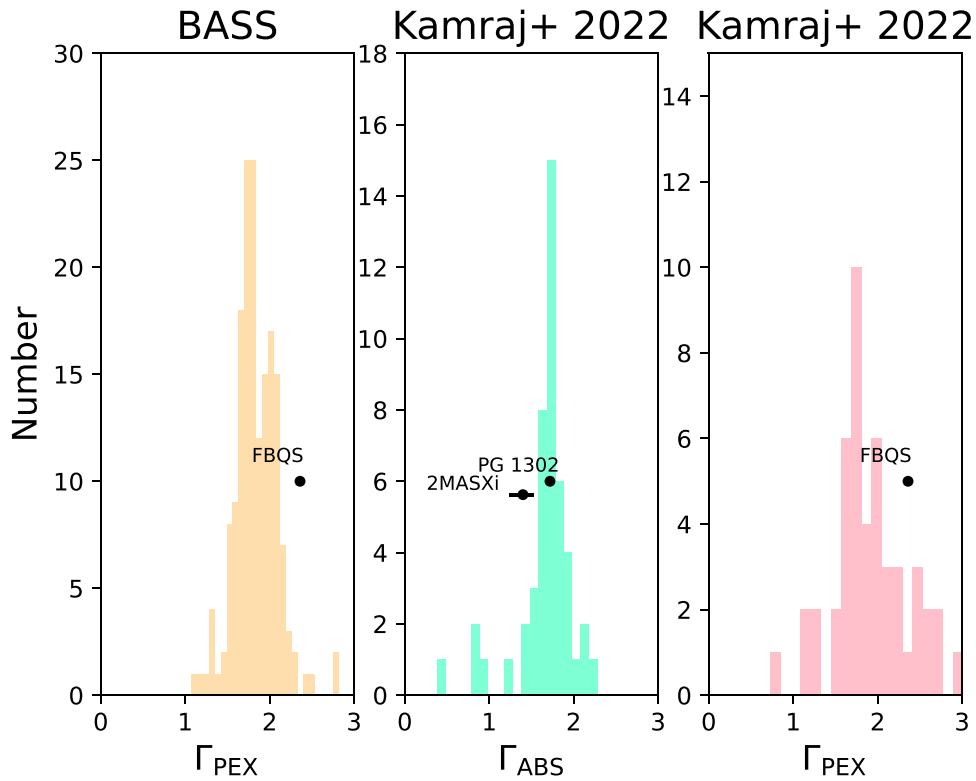


Figure 4. Spectral indices derived from average spectra for the three AGN in our sample compared to histograms of the comparison samples used for the KS test. The histograms themselves depict Γ values from the BASS sample (Ricci et al. 2017; left panel), Γ_{ABS} values from Kamraj et al. (2022; middle panel), and Γ_{PEX} values from Kamraj et al. (2022; right panel). The leftmost panel and rightmost panel use the Γ from the average TBABS*ZPHABS*(CUTOFFPL+PEXRAV) fit of FBQS J163302.6+234928. The middle panel uses Γ from the average TBABS*ZPHABS*CUTOFFPL fit of 2MASXi J0729087+400836 and PG 1302–102. In all three cases, the candidate binary SMBH AGN are not substantially distinct from the larger general AGN populations.

matched Table 1 in Kamraj et al. (2022) with the BAT 70 month survey (Baumgartner et al. 2013) as well as Ricci et al. (2017) to retrieve 2–10 keV luminosities and Koss et al. (2017) to retrieve Eddington ratios. Kamraj et al. (2022) fit the AGN with models including just a CUTOFFPL component, models with a CUTOFFPL+PEXRAV component, and models with an XILLVERCP component. We performed a KS test to compare our measured spectral indices to the spectral indices in Table 1 of Kamraj et al. (2022), specifically the ones measured using a phenomenological reflection (PEXRAV) model. There were a total of 103 AGN with Γ values measured using the PEXRAV-containing model. The 103 AGN with the PEXRAV model are in the range $0.002 \leq z \leq 0.197$, with bolometric luminosities $42.44 \leq \log(L_{\text{bol}}/\text{erg s}^{-1}) \leq 46.61$. Multiple fits were listed for some AGN, so where there were duplicates, we chose the fit with the C-stat/dof value closest to 1. We find that 67 of the AGN with Γ values had Eddington ratios listed in Koss et al. (2017). We made the same cut on the Eddington ratio as we did for our test versus the BASS sample, $-1.08 \leq \log(L/L_{\text{Edd}}) \leq -0.08$. This left a total of 49 AGN in the sample. After performing the KS test grouping our sample as a distribution versus the Kamraj et al. (2022) sample, the resulting p -value was 0.990. We cannot reject the null hypothesis that our values of Γ are drawn from the same distribution as the Γ_{PEX} values of Kamraj et al. (2022). The values of Γ for all three sources are plotted against histograms of Γ values for the comparison samples used in the KS test in Figure 4.

It is worth comparing the very high value of R of FBQS J163302.6+234928 to the values of R of the BASS

sample as well. When compared to all nonblazar AGN in the BASS sample with measured R values (184 AGN), there are only two AGN with R values greater than or equal to the 90% confidence interval for FBQS J163302.6+234928, namely, Mrk 1310 with $R = 6.7$ and ESO 438–9 with $R = 7.8$.

At energies below ~ 1 keV, emission from the viscously heated circumbinary disk dominates, while the higher-energy spectrum is dominated by shock-heated gas in the minidisks around each SMBH, streams, and near the cavity wall at the inner edge of the circumbinary disk. The presence of the cavity could lead to a small depression at a few keV (e.g., Tang et al. 2018) where the cavity in the circumbinary disk cuts out a range of temperatures. However, as explained in Tang et al. (2018), their simulations are initialized with an artificially high disk temperature for numerical reasons. A single-black-hole disk with similar parameters, experiencing only viscous heating, would be 10–100 times cooler, moving the notch to correspondingly lower photon energies. Additional heating by the binary through shocks could maintain a high disk temperature and cause a depression in the X-ray region, but future work is required to assess this. In any case, as seen in the unfolded X-ray spectra presented in Figures 1–3, there is no evidence of notches in the high-energy spectra of any of the sources. This could be due to the notch signature being too subtle for the signal-to-noise ratio of our data or due to the sources not in fact being binary SMBH AGN. Alternatively, theoretical work based on viscous heating of a standard geometrically thin, optically thick single-black-hole disk (i.e., without shock heating due to a binary) predicts the notch to be at much lower energies, in the UV/optical/IR range (Roedig

Table 3
Parameters for the Best TBABS*ZPHABS (CUTOFFPL+PEXRAV) Fit with Varying Spectral Parameters for FBQS J163302.6+234928

Obs. Date	ZPHABS	CUTOFFPL			PEXRAV	C-stat/dof
	N_{H} (10^{22} cm^{-2})	Γ	E_{cut} (keV)	Norm ($10^{-4} \text{ counts s}^{-1} \text{ keV}^{-1}$)	R	
2020-08-08	0.14 ± 0.01	2.22 ± 0.05	$64.26^{+15.10}_{-10.46}$	$4.54^{+0.23}_{-0.22}$	$4.97^{+1.22}_{-1.02}$	3015.037/2912
2021-01-31		2.40 ± 0.05			$8.83^{+1.56}_{-1.37}$	

Note. Error bars represent 90% confidence intervals. Abundances were set to solar, the PEXRAV cutoff energy was set equal to the CUTOFFPL cutoff energy, and the PEXRAV norm was set equal to the CUTOFFPL norm, leaving R as the only free PEXRAV parameter. The XMM-Newton normalization constants for the first observation of FBQS J163302.6+234928 (ObsID: 0870910101) were $0.80^{+0.04}_{-0.03}$ for pn, 0.69 ± 0.05 for MOS1, and $0.86^{+0.08}_{-0.07}$ for MOS2. The XMM-Newton normalization constants for the second observation of FBQS J163302.6+234928 (ObsID: 0870910301) were 1.12 ± 0.05 for pn, 1.15 ± 0.06 for MOS1, and 1.15 ± 0.06 for MOS2. The NuSTAR FPMA constant for the second observation of FBQS J163302.6+234928 (ObsID: 60601012004) was 1.18 ± 0.07 .

Table 4
Parameters for the Best TBABS*ZPHABS*CUTOFFPL Fit with Varying Spectral Parameters for 2MASXi J0729087+400836

Obs. Date	ZPHABS	CUTOFFPL			C-stat/dof
	N_{H} (10^{22} cm^{-2})	Γ	E_{cut} (keV)	Norm ($10^{-4} \text{ counts s}^{-1} \text{ keV}^{-1}$)	
2017-04-28	$0.27^{+0.20}_{-0.09}$	$1.33^{+0.23}_{-0.06}$	>69.5	$4.81^{+0.89}_{-0.83}$	1030.36/1143
2021-05-16		$1.51^{+0.13}_{-0.08}$			

Note. Error bars represent 90% confidence intervals. The Chandra normalization constant for the first observation of 2MASXi J0729087+400836 (ObsID: 19528) is $1.19^{+0.30}_{-0.23}$.

et al. 2014; Krolik et al. 2019). The shape and depth of the notch are also highly dependent on the binary parameters of the system. For example, Roedig et al. (2014) express the temperature of the thermal emission that would be missing because of the notch in their Equation (2),

$$T_0 = 3.3 \times 10^4 [\dot{m}(\eta/0.1)^{-1} M_8^{-1} (a/100R_g)^{-3}]^{1/4} \text{ K}, \quad (1)$$

where \dot{m} is the accretion rate in Eddington units, η is the radiative efficiency, and M_8 is the black hole mass in units of $10^8 M_{\odot}$. Using the mass and binary separations of our sample (listed in Table 3 of SA20) and the Eddington ratios listed in Table 5 of this paper, assuming that the binary separation is a , and assuming a radiative efficiency of 0.1, the resulting temperatures are 2334 K for 2MASXi J0729087+400836, 6836 K for PG 1302–102, and 10,547 K for FBQS J163302.6+234928. This would place the notch in the optical part of the spectrum for 2MASXi J0729087+400836 and the ultraviolet part of the spectrum for PG 1302–102 and FBQS J163302.6+234928.

We also tested fits to these AGN with two power-law components representing the continuum instead of a single power-law component, under the assumption that if two black holes were present, their coronae would not necessarily have the same spectral indices. As expected for the additional degree of freedom, we did get improvements in the C-stat/dof, but the power law invariably became extremely soft, much steeper than the expectations of coronal emission. This suggested that the additional parameter was picking up a soft excess component of the spectrum, rather than a second corona. We added a third power law to the fits, but they did not improve the C-stat/dof. We therefore do not find any evidence of two coronae in these data.

3.2. Spectral and Flux Variability

There is the potential for spectral variability between the different epochs of observation of 2MASXi J0729087+400836 and FBQS J163302.6+234928. For FBQS J163302.6+234928, we tested fits where ZPHABS N_{H} , CUTOFFPL Γ and E_{cut} , and PEXRAV R varied. We found that including variability in Γ and R improved the fits, while including variability in the others did not. We tabulate the results of the best TBABS*ZPHABS*(CUTOFFPL+PEXRAV) fit with Γ and R free to vary in Table 3. The latter is also plotted as the model in Figure 1. The value of Γ in these fits becomes softer when the source is brighter, which is consistent with the well-established correlation between Γ and the Eddington ratio (e.g., Brightman et al. 2013). During the first epoch, R is more in line with the range of R values seen in the BASS sample, with 14 AGN possessing R values within its 90% confidence interval, plus two that exceed it. However, the second-epoch R reached an even higher value than in the average fit, $8.83^{+1.56}_{-1.37}$. Only one BASS AGN has an R value within this 90% confidence interval. As with the average spectrum, we set an upper limit of 2 on R and refit to see if the value of Γ would become harder, but it only went down to 2.04 ± 0.03 in the first epoch and 2.14 ± 0.02 in the second epoch. We also tried ignoring energies of $<2 \text{ keV}$, but in this case, Γ was only $2.03^{+0.15}_{-0.14}$ in the first epoch and 2.01 ± 0.11 in the second epoch, which are still soft values.

For 2MASXi J0729087+400836, we found that allowing Γ to vary between epochs improved the fit, while allowing the other spectral parameters to vary did not. The best TBABS*ZPHABS*CUTOFFPL fit with varying Γ is tabulated in Table 4. The source is harder in the Chandra observation than in the NuSTAR observations, also consistent with the prevailing trend of harder gamma values with increasing Eddington ratio. Since the 90% confidence intervals of Γ overlap between the

Table 5
Table of AGN Properties

Target	Obs. Date	z	f_{2-10}^a	$\log(L_{2-10})^b$	L/L_{Edd}^c
2MASXi J0729087+400836	Avg.	0.074	$22.91_{-1.0}^{+1.1}$	43.52 ± 0.02	0.08
	2017-04-28		$23.4_{-2.5}^{+0.6}$	$43.50_{-0.02}^{+0.04}$	0.08
	2021-05-16		24.6 ± 1.7	43.55 ± 0.03	0.09
PG 1302–102	2021-06-08	0.278	$38.90_{-0.89}^{+1.83}$	45.01 ± 0.01	0.76
FBQS J163302.6+234928	Avg.	0.821	$8.51_{-0.19}^{+0.20}$	45.46 ± 0.01	0.13
	2020-08-08		9.12 ± 0.21	45.49 ± 0.01	0.15
	2021-01-31		$12.30_{-0.20}^{+0.30}$	45.62 ± 0.10	0.20

Notes.

^a Model flux from rest-frame 2–10 keV, in units of 10^{-13} erg cm $^{-2}$ s $^{-1}$. Measured from the CUTOFFPL component of the TBABS*ZPHABS*CUTOFFPL fit for 2MASXi J0729087+400836 and PG 1302–102 and from the CUTOFFPL and PEXRAV components of the TBABS*ZPHABS*(CUTOFFPL+PEXRAV) fit for FBQS J163302.6+234928.

^b Calculated using flux from previous column, in units of erg s $^{-1}$.

^c Calculated using bolometric correction $K_X(L_X)$ from Table 1 of Duras et al. (2020) and the black hole masses listed in Table 3 of SA20.

two epochs, the evidence for spectral variability in this source is weaker than for FBQS J163302.6+234928.

PG 1302–102 had a single set of simultaneous Swift and NuSTAR observations, so we did not attempt to fit it with a model that had parameters vary between the observations. We plot its average spectrum in Figure 2 using the fit from Table 2.

The rest-frame 2–10 keV fluxes for the AGN in our sample were measured from the CUTOFFPL component in 2MASXi J0729087+400836 and PG 1302–102 and from the sum of the CUTOFFPL and PEXRAV components in FBQS J163302.6+234928. From these, we derived the rest-frame 2–10 keV luminosities using the luminosity distances listed in NED. These are tabulated in Table 5. We then calculated the bolometric luminosities using the rest-frame 2–10 keV luminosity and the universal expression for the bolometric correction $K_X(L_X)$ from Table 1 of Duras et al. (2020). Finally, the bolometric luminosities were divided by the Eddington luminosity for each object, which was estimated using $L_{\text{Edd}} = 1.26 \times 10^{38} (M_{\text{BH}}/M_{\odot})$ erg s $^{-1}$. The SMBH masses were derived from Table 3 of SA20. The rest-frame 2–10 keV luminosities and the Eddington ratios are also listed in Table 5. For 2MASXi J0729087+400836 and FBQS J163302.6+234928, we include the epoch-by-epoch fluxes, luminosities, and Eddington ratios as separate lines in Table 5.

4. Discussion

Roedig et al. (2014) predict that binary SMBH systems will have excess shock-heated gas with a temperature on the order of ~ 100 keV for a separation of $\sim 100r_g$, where the gravitational radius $r_g \equiv GM/c^2$, G is the gravitational constant, M is the total binary mass, and c is the speed of light. This gas is heated by the impact of narrow streams of accreting material as they fall from the circumbinary disk into the minidisks around the individual black holes. This would lead to a thermal component to the X-ray spectrum separate from the standard coronal power law. Following Roedig et al. (2014), we can estimate the temperature of the shocked gas of the binary SMBH using their Equation (12), i.e.,

$$T_{s1,2} = 6.2 \times 10^{10} [(1.4 + 1.2Zm_e/m_p)/(1.1 + 1.2Z)] \times (a/100R_g)^{-1} \Phi_{1,2}^2 (1 + q)^{-1} (q^{0.3}, q^{0.7}) \text{ K}, \quad (2)$$

where the 1, 2 notation denotes the primary or secondary black hole, and Z is the ratio of leptons to protons. Φ is a factor of order unity, with $\Phi_1 \simeq 0.9$ for the primary and $\Phi_2 \simeq 0.6$ for the secondary, assuming a binary mass ratio of 0.3. Using values for a from SA20 and the redshifts of the AGN and assuming $q = 0.3$ and $Z = 1$, we can find observed frame energies for the shock-heated gas around each individual black hole. These energies are 78.6 keV (primary) and 21.6 keV (secondary) for 2MASXi J0729087+400836, 275 keV (primary) and 75 keV (secondary) for PG 1302–102, and 2.48 MeV (primary) and 680.81 keV (secondary) for FBQS J163302.6+234928. While most of these energies are outside the observational range of NuSTAR, the energy for the secondary of 2MASXi J0729087+400836 is within the detectable range. Roedig et al. (2014) note, however, that these values are upper limits because cooling via efficient electron/positron pair production could decrease the temperature of the shocked gas. This raises the possibility that the excess energy in PG 1302–102 and FBQS J163302.6+234928, as well as from the primary of 2MASXi J0729087+400836, would be detectable in the X-ray data considered here. The uncertainty as to the excess's true location means we cannot definitely state whether we have detected it or not. Detecting the excess X-ray emissions due to shocked accretion streams would be difficult even if the temperatures were low enough to be in the soft X-ray or NuSTAR bands. A soft X-ray excess would resemble the soft excess seen in many single SMBH AGN, while a hard X-ray excess would resemble the Compton reflection component also seen in many single SMBH AGN. If the soft excess seen in single SMBH AGN is blurred reflection, an observatory with high spectral resolution like XRISM (XRISM Science Team 2020) would likely be able to tell it apart from a thermal soft excess expected as a result of emission from the accretion streams and minidisks.

The case of a hard excess from a binary mimicking an enhanced reflection component is particularly relevant for FBQS J163302.6+234928, which shows an extremely high value of R in both its average spectrum and especially the second epoch. This could potentially be evidence of excess hard X-ray emission from a binary SMBH. However it should be noted that even its high R value is not entirely out of the

range known from single SMBH AGN. In particular, Mrk 1310 and ESO 438-9 in the BASS sample show R values of 6.7 and 7.8, respectively, and neither is known to be a binary SMBH candidate. Even during the second epoch, FBQS J163302.6+234928 is less than 3σ away from ESO 438-9. So while the very hard spectrum of FBQS J163302.6+234928 is interesting, it cannot be conclusively stated to be outside the range of normal AGN.

The predicted binary separations for these sources (listed in Table 3 of SA20) are all too small to place the enhanced X-ray emission in the NuSTAR band, with the exception of the secondary's minidisk for 2MASX J0729087+400836. While 2MASX J0729087+400836 does have a slightly harder spectrum than typical for an AGN, the difference is not statistically significant. The absence of hardening in 2MASX J0729087+400836's spectra investigated in this paper potentially implies that cooling due to pair production is inefficient.

We have shown that broadband X-ray spectra, spanning the soft X-rays observed by Chandra, Swift, and XMM-Newton to the hard X-rays observed by NuSTAR, do not exhibit any evidence that the three candidate binary SBMH AGN studied here are dramatically different from the typical (single) AGN population. The broadband X-ray spectral indices are not distinct from larger AGN populations, despite some theoretical predictions that enhanced X-ray emission should be expected. We find no evidence for a notch in their X-ray spectra, nor do we find evidence for multiple X-ray coronae. There are multiple potential explanations for this nonresult. First, the signatures of a binary SMBH might be too subtle given the quality of our data. In that case, deeper observations or future, more sensitive facilities might detect indications of binarity missed in the current data. Second, as emphasized in SA20, theoretical predictions of high-energy emission from binary SMBH AGN are relatively immature as a field, with models still highly idealized. In that case, observations such as these test current models and will help direct future theoretical modeling.

Finally, it is possible the three AGN investigated in this paper are not in fact binary SMBHs. Indeed, we know that not all binary SMBH candidates can truly be binaries, since this would overpredict the gravitational-wave background seen by pulsar timing arrays (Sesana et al. 2018). The literature is rife with claimed periodicity in AGN light curves, though follow-up analyses find many claims to be statistically lacking (e.g., Vaughan et al. 2016; Barth & Stern 2018). Recent work shows that PG 1302–102's variations cannot be explained by random noise, and there is very strong support for periodicity, or at least quasiperiodicity (Zhu & Thrane 2020), where the latter is an expected consequence of SMBH binaries (Bowen et al. 2019; Combi et al. 2022). We also note that even if the periodicity (or quasiperiodicity) is real, it might not be due to a binary SMBH system. Similar to the mechanism that causes quasiperiodic oscillations in systems with a stellar-mass compact object (e.g., Zhu & Thrane 2020), periodicity could potentially be due to precession of the accretion disk or jet (e.g., Dotti et al. 2023). However, as noted by Graham et al. (2015b), the timescale for a warped accretion disk (such that it would undergo precession) to remain before self-gravity undoes the warp is much shorter than the typical AGN lifetime. It is therefore unlikely that precession due to a warped

accretion disk explains the behavior of the three AGN studied here.

Ongoing and future synoptic surveys will improve and extend the light curves for candidate periodic AGN, testing their unusual variability with increasing statistical accuracy. In particular, De Rosa et al. (2019) mention that the Rubin Observatory will scan the entire observable optical sky every 3 days and will be able to monitor 10^4 – 10^5 AGN in the Deep Drilling Fields with an even higher cadence. It will be by far the best survey in terms of signal-to-noise, sampling, and duration for identifying and confirming periodic AGN candidates.

Some current candidates will likely fall as a result of additional monitoring, while new candidates will be identified. X-ray emission, coming from the innermost regions around the SMBH(s), should, in principle, provide a strong test if the observed periodicity is due to binarity. Our results, emphasizing soft X-ray data in SA20 and broadband X-ray data here, do not find evidence for unusual X-ray properties for some of the strongest and X-ray-brightest binary SMBH candidates currently known. However, we are still in the early stages of this field, both observationally and theoretically. The nondetections reported here can help motivate future, more sensitive observations (and observatories), while simultaneously helping direct theoretical work.



Acknowledgments


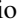

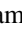







We thank Julian Krolik for helpful comments that have improved the paper. The scientific results reported in this article are based on data obtained from the Chandra Data Archive. This work is based on observations obtained with XMM-Newton, an ESA science mission with instruments and contributions directly funded by ESA Member States and NASA. We acknowledge the use of public data from the Swift data archive. The scientific results reported in this paper are based on data obtained from the Chandra Data Archive (ObsID 19528). This research has made use of data and/or software provided by the High Energy Astrophysics Science Archive Research Center (HEASARC), which is a service of the Astrophysics Science Division at NASA/GSFC and the High Energy Astrophysics Division of the Smithsonian Astrophysical Observatory. This work has made use of data obtained from the NuSTAR mission, a project led by Caltech, funded by NASA, and managed by NASA/JPL. D.J.D. received funding from the European Union's Horizon 2020 research and innovation program under Marie Skłodowska-Curie grant agreement No. 101029157 and from the Danish Independent Research Fund through Sapere Aude Starting grant No. 121587. Z.H. acknowledges support from NASA ATP grant 80NSSC22K082.

Facilities: CXO, NuSTAR, XMM, Swift.

Software: HEASOFT (Nasa High Energy Astrophysics Science Archive Research Center (Heasarc), 2014), CIAO (Fruscione et al. 2006), XMM-Newton SAS (Gabriel et al. 2004).

ORCID iDs

M. Lynne Saade  <https://orcid.org/0000-0001-7163-7015>
 Murray Brightman  <https://orcid.org/0000-0002-8147-2602>
 Daniel Stern  <https://orcid.org/0000-0003-2686-9241>
 Thomas Connor  <https://orcid.org/0000-0002-7898-7664>

S. G. Djorgovski  <https://orcid.org/0000-0002-0603-3087>
 Daniel J. D’Orazio  <https://orcid.org/0000-0002-1271-6247>
 K. E. S. Ford  <https://orcid.org/0000-0002-5956-851X>
 Matthew J. Graham  <https://orcid.org/0000-0002-3168-0139>
 Zoltán Haiman  <https://orcid.org/0000-0003-3633-5403>
 Hyunsung D. Jun  <https://orcid.org/0000-0003-1470-5901>
 Elias Kammoun  <https://orcid.org/0000-0002-0273-218X>
 Ralph P. Kraft  <https://orcid.org/0000-0002-0765-0511>
 Barry McKernan  <https://orcid.org/0000-0002-9726-0508>
 Alexei Vikhlinin  <https://orcid.org/0000-0001-8121-0234>
 Dominic J. Walton  <https://orcid.org/0000-0001-5819-3552>

References

- Amaro-Seoane, P., Audley, H., Babak, S., et al. 2017, arXiv:1702.00786
 Amaro-Seoane, P., Andrews, J., Arca Sedda, M., et al. 2023, *LRR*, 26, 2
 Arnaud, K. A. 1996, in ASP Conf. Ser. 101, *Astronomical Data Analysis Software and Systems V*, ed. G. H. Jacoby & J. Barnes (San Francisco, CA: ASP), 17
 Ballantyne, D. R., & Xiang, X. 2020, *MNRAS*, 496, 4255
 Barth, A. J., & Stern, D. 2018, *ApJ*, 859, 10
 Baumgartner, W. H., Tueller, J., Markwardt, C. B., et al. 2013, *ApJS*, 207, 19
 Begelman, M. C., Blandford, R. D., & Rees, M. J. 1980, *Natur*, 287, 307
 Berezhik, P., Merritt, D., Spurzem, R., & Bischof, H.-P. 2006, *ApJL*, 642, L21
 Bogdanović, T., Miller, M. C., & Blecha, L. 2022, *LRR*, 25, 3
 Bowen, D. B., Mewes, V., Noble, S. C., et al. 2019, *ApJ*, 879, 76
 Brightman, M., Silverman, J. D., Mainieri, V., et al. 2013, *MNRAS*, 433, 2485
 Caproni, A., Abraham, Z., & Monteiro, H. 2013, *MNRAS*, 428, 280
 Charisi, M., Bartos, I., Haiman, Z., et al. 2016, *MNRAS*, 463, 2145
 Chen, Y.-C., Liu, X., Liao, W.-T., et al. 2020, *MNRAS*, 499, 2245
 Chen, Y.-J., Zhai, S., Liu, J.-R., et al. 2024, *MNRAS*, 527, 12154
 Combi, L., Lopez Armengol, F. G., Campanelli, M., et al. 2022, *ApJ*, 928, 187
 Crummy, J., Fabian, A. C., Gallo, L., & Ross, R. R. 2006, *MNRAS*, 365, 1067
 d’Ascoli, S., Noble, S. C., Bowen, D. B., et al. 2018, *ApJ*, 865, 140
 De Rosa, A., Vignali, C., Bogdanović, T., et al. 2019, *NewAR*, 86, 101525
 Done, C., Davis, S. W., Jin, C., Blaes, O., & Ward, M. 2012, *MNRAS*, 420, 1848
 D’Orazio, D. J., Haiman, Z., & Schiminovich, D. 2015, *Natur*, 525, 351
 Dotti, M., Bonetti, M., Rigamonti, F., et al. 2023, *MNRAS*, 518, 4172
 Drake, A. J., Djorgovski, S. G., Mahabal, A., et al. 2009, *ApJ*, 696, 870
 Duras, F., Bongiorno, A., Ricci, F., et al. 2020, *A&A*, 636, A73
 Eracleous, M., Boroson, T. A., Halpern, J. P., & Liu, J. 2012, *ApJS*, 201, 23
 Farris, B. D., Duffell, P., MacFadyen, A. I., & Haiman, Z. 2015, *MNRAS*, 447, L80
 Fruscione, A., McDowell, J. C., Allen, G. E., et al. 2006, *Proc. SPIE*, 6270, 62701V
 Gabriel, C., Denby, M., Fyfe, D. J., et al. 2004, in ASP Conf. Ser. 314, *Astronomical Data Analysis Software and Systems (ADASS) XIII*, ed. F. Ochsenbein, M. G. Allen, & D. Egret (San Francisco, CA: ASP), 759
 Gehrels, N., Chincarini, G., Giommi, P., et al. 2004, *ApJ*, 611, 1005
 Graham, M. J., Djorgovski, S. G., Stern, D., et al. 2015a, *Natur*, 518, 74
 Graham, M. J., Djorgovski, S. G., Stern, D., et al. 2015b, *MNRAS*, 453, 1562
 Gualandris, A., Read, J. I., Dehnen, W., & Bortolas, E. 2017, *MNRAS*, 464, 2301
 Guo, H., Liu, X., Shen, Y., et al. 2019, *MNRAS*, 482, 3288
 Gutiérrez, E. M., Combi, L., Noble, S. C., et al. 2022, *ApJ*, 928, 137
 Harrison, F. A., Craig, W. W., Christensen, F. E., et al. 2013, *ApJ*, 770, 103
 Jansen, F., Lumb, D., Altieri, B., et al. 2001, *A&A*, 365, L1
 Ju, W., Greene, J. E., Rafikov, R. R., Bickerton, S. J., & Badenes, C. 2013, *ApJ*, 777, 44
 Jun, H. D., Stern, D., Graham, M. J., et al. 2015, *ApJL*, 814, L12
 Kamraj, N., Brightman, M., Harrison, F. A., et al. 2022, *ApJ*, 927, 42
 Komossa, S., Grupe, D., Kraus, A., et al. 2023, *MNRAS*, 522, L84
 Komossa, S., Grupe, D., Parker, M. L., et al. 2020, *MNRAS*, 498, L35
 Koss, M., Trakhtenbrot, B., Ricci, C., et al. 2017, *ApJ*, 850, 74
 Krause, M. G. H., Shabala, S. S., Hardcastle, M. J., et al. 2019, *MNRAS*, 482, 240
 Krolik, J. H., Volonteri, M., Dubois, Y., & Devriendt, J. 2019, *ApJ*, 879, 110
 Kun, E., Gabányi, K. É., Karouzos, M., Britzen, S., & Gergely, L. Á. 2014, *MNRAS*, 445, 1370
 Lehto, H. J., & Valtonen, M. J. 1996, *ApJ*, 460, 207
 Li, Y.-R., Wang, J.-M., Ho, L. C., et al. 2016, *ApJ*, 822, 4
 Liao, W.-T., Chen, Y.-C., Liu, X., et al. 2021, *MNRAS*, 500, 4025
 Liu, T., Gezari, S., Ayers, M., et al. 2019, *ApJ*, 884, 36
 Liu, T., Koss, M., Blecha, L., et al. 2020, *ApJ*, 896, 122
 Liu, X., Shen, Y., Bian, F., Loeb, A., & Tremaine, S. 2014, *ApJ*, 789, 140
 Lobanov, A. P., & Roland, J. 2005, *A&A*, 431, 831
 Madsen, K. K., Harrison, F. A., Markwardt, C. B., et al. 2015, *ApJS*, 220, 8
 Magdziarz, P., & Zdziarski, A. A. 1995, *MNRAS*, 273, 837
 Mayer, L., Kazantzidis, S., Madau, P., et al. 2007, *Sci*, 316, 1874
 Mehdipour, M., Branduardi-Raymont, G., Kaastra, J. S., et al. 2011, *A&A*, 534, A39
 Nandra, K., & Pounds, K. A. 1994, *MNRAS*, 268, 405
 Nasa High Energy Astrophysics Science Archive Research Center (Heasarc), 2014 HEASoft: Unified Release of FTOOLS and XANADU, Astrophysics Source Code Library, ascl:1408.004
 O’Neill, S., Kiehlmann, S., Readhead, A. C. S., et al. 2022, *ApJL*, 926, L35
 Qian, S. J., Britzen, S., Witzel, A., Krichbaum, T. P., & Kun, E. 2018, *A&A*, 615, A123
 Ricci, C., Trakhtenbrot, B., Koss, M. J., et al. 2017, *ApJS*, 233, 17
 Roedig, C., Krolik, J. H., & Miller, M. C. 2014, *ApJ*, 785, 115
 Ryan, G., & MacFadyen, A. 2017, *ApJ*, 835, 199
 Saade, M. L., Stern, D., Brightman, M., et al. 2020, *ApJ*, 900, 148
 Serafinelli, R., Severgnini, P., Braitto, V., et al. 2020, *ApJ*, 902, 10
 Sesana, A., Haiman, Z., Kocsis, B., & Kelley, L. Z. 2018, *ApJ*, 856, 42
 Shemmer, O., Brandt, W. N., Netzer, H., Maiolino, R., & Kaspi, S. 2008, *ApJ*, 682, 81
 Shen, Y., Liu, X., Loeb, A., & Tremaine, S. 2013, *ApJ*, 775, 49
 Tang, Y., Haiman, Z., & MacFadyen, A. 2018, *MNRAS*, 476, 2249
 Tsai, C.-W., Jarrett, T. H., Stern, D., et al. 2013, *ApJ*, 779, 41
 Valtonen, M. J., Lehto, H. J., Nilsson, K., et al. 2008, *Natur*, 452, 851
 Vaughan, S., Uttley, P., Markowitz, A. G., et al. 2016, *MNRAS*, 461, 3145
 Walton, D. J., Nardini, E., Fabian, A. C., Gallo, L. C., & Reis, R. C. 2013, *MNRAS*, 428, 2901
 Weisskopf, M. C., Brinkman, B., Canizares, C., et al. 2002, *PASP*, 114, 1
 Xin, C., Charisi, M., Haiman, Z., et al. 2020, *MNRAS*, 496, 1683
 Xin, C., Mingarelli, C. M. F., & Hazboun, J. S. 2021, *ApJ*, 915, 97
 XRISM Science Team 2020, arXiv:2003.04962
 Zhu, X.-J., & Thrane, E. 2020, *ApJ*, 900, 117